Supplementary Information for: Vibrational coupling infrared nano-crystallography

Richard Puro,[1] Thomas Gray,[1] Tsitsi A. Kapfunde,[2]

George B. Richter-Addo,[2] and Markus B. Raschke[1,*]

[1]*Department of Physics and JILA, University of Colorado, Boulder, CO, 80309, USA*

[2]*Department of Chemistry and Biochemistry,*

University of Oklahoma, Norman, OK 73019, USA

MATERIALS AND METHODS

Preparation of (OEP)Ru(CO)(DMPO): (OEP)Ru(CO) and 5,5-dimethyl-l-pyrroline N-oxide (DMPO, 97%) were purchased from MidCentury Chemicals and Sigma-Aldrich, respectively, and used as received. Chloroform-d (99.8%) was purchased from Cambridge Isotope Laboratories and dried using activated 4 Å molecular sieves. Solvents used in the reactions were dispensed under N_2 from a PureSolv 400-5-MD Solvent Purification System (Innovative Technology).

The title compound was synthesized according to a published literature procedure [1]. Excess DMPO (100 mg, 0.88 mmol) was added to a toluene (12 ml) solution of (OEP)Ru(CO) (46 mg, 0.069 mmol) under a nitrogen atmosphere, and the solution was heated under reflux for 30 min, during which it turned from red to dark red. The solvent was removed in vacuo, and the residue was transferred to the glovebox and redissolved in 5 ml CH_2Cl_2. The solution was transferred to a vial and layered with 5 ml hexane. Slow evaporation of the solution under a nitrogen atmosphere (glovebox) resulted in the generation of small red crystals which were washed with hexane (10 ml) and dried in vacuo to give the product (OEP)Ru(CO)(DMPO), (0.029 g, 0.037 mmol, 54% isolated yield). A suitable crystal for XRD structure determination was grown by slow evaporation from toluene/heptane (1:1) solution at room temperature under inert atmosphere.

To comfirm the identity of the synthesized compound, FTIR spectra were recorded on a Bruker Tensor 27 spectrometer. NMR spectroscopy was performed on a 400 MHz Varian NMR spectrometer. ^{1}H signals were referenced to the residual signal of the solvent employed ($CHCl_3$ at δ = 7.26 ppm). Solution IR (CH_2Cl_2, cm^{-1}): ν_{CO} = 1914, IR (KBr, cm^{-1}): ν_{CO} = 1914, IR (NaCl, cm^{-1}): ν_{CO} = 1913. ^{1}H NMR ($CDCI_3$, -30 degC): (δ, ppm) 9.84 (s, 4H. *meso*-H of OEP), 2.36 (s, toluene), 1.87 (t, J = 8 Hz, 24H, CH_2CH_3 of OEP), 0.67 (m, 2H of DMPO), 0.21 (m, overlapping 1H and 2H of DMPO), -1.63 (s, 6H, cH_3 of DMPO).

The structure of (OEP)Ru(CO)(DMPO) crystals has been resolved previously [1]. Unit cell dimensions measured are slightly smaller than those previously published by $<$0.2 Å, likely due to thermal contraction. We choose to use the crystal parameters previously published for modeling because the R-factor of the measurements on new crystals (R_{int} = 0.1133) was significantly higher than what was published and the temperature was further from room temperature, at which IR *s*-SNOM measurements were performed. However, the agreement between the newly measured structure and previously published structure confirms the molecules are arranged in the same crystal structure.

IR *s*-SNOM: IR *s*-SNOM was performed using an atomic force microscope (AFM) (customized nanoIR2-s prototype, Anasys Instruments/Bruker) with an asymmetric Michelson interferometer as described previously [2, 3]. 10 mW of femtosecond mid-IR light, tunable from 5 - 10 μm (Flint, Light Conversion; Levante OPO and HarmoniXX DFG, APE), was attenuated by 50% with a mesh filter before reaching the beam splitter of the interferometer. The laser spectrum was centered on $\tilde{\nu}^c_{CO}$ (1921 cm^{-1}) and had a FWHM bandwidth of $\sim$100 cm^{-1}. One arm of the interferometer was directed to an off axis parabolic mirror (NA = 0.45), which focused the light onto a metalized AFM tip (160AC-GG OPUS, MikroMasch). The tip back scattered light was detected with a HgCdTe detector (MCT KLD-0.5-J1/DC/11, Kolmar Technologies). This signal was lock-in demodulated (Zurich Instruments HF2LI) at the second-harmonic of the tip tapping frequency. Each IR *s*-SNOM spectrum was recorded in 50 seconds.

X-ray diffraction: A purple, needle-shaped crystal of dimensions 0.042 x 0.060 x 0.340 mm was selected for structural analysis. The selected crystal was a three-component twinned crystal. The displacement ellipsoids were drawn at the 50% probability level. Intensity data for this compound were collected using a D8 Quest κ-geometry diffractometer with a Bruker Photon II cmos area detector and an Incoatec Iμs microfocus Mo Kα source (λ = 0.71073 Å). The sample was cooled to 100(2) K. Cell parameters were determined from a least-squares fit of 9927 reflections in the range $2.66 < \Theta < 26.20°$. a total of 124473 peaks were measured in the range $2.584 < \Theta < 25.677°$ using ϕ and ω oscillation frames. The data were corrected for absorption by the empirical method [4] giving minimum and maximum transmission factors of 0.673 and 0.745. The data were merged to form a set of 116153 independent reflections with R_{int} = 0.1133 and a coverage of 99.7%.

The monoclinic space group *Pn* was determined by systematic absences and statistical tests and verified by subsequent refinement. The structure was solved by dual-space methods and refined by full-matrix least-squares methods on F^2 [5]. The positions of hydrogens bonded to carbons were initially determined by geometry and were refined using a riding model. Non-hydrogen atoms were refined with anisotropic displacement parameters. Hydrogen atom displacement parameters were set to 1.2 (1.5 for methyl) times the isotropic equivalent displacement parameters of the bonded atoms. A total of 462 parameters were refined against 484 restraints and 116153 reflections to give $wR(F^2)$ = 0.2710 and S = 1.002 for weights of $w = 1/[\sigma^2(F^2) + (0.0920\ P)^2 + 6.1000\ P]$, where $P = [F_0^2 + 2F_c^2]/3$. The final R(F) was 0.0972 for the 78171 observed, $[F > 4\sigma(F)]$, data. The largest shift/s.u. was 0.003 in the final refinement cycle. The final difference map had maxima

Empirical formula	$C_{45}H_{55}N_5O_2Ru$	
Formula weight	774.99	
Crystal system	monoclinic	
Space group	*Pn*	
Unit cell dimensions	a=8.2899(12) Å	α=90°
	b=10.4645(19) Å	β=92.503°
	c=22.435(4) Å	γ=90°
Unit cell volume	1944.4(6) Å^3	
Z, Z'	2, 1	
Density	1.324 mg/m^3	
Wavelength	0.71073 Å	
Temperature	100(2) K	
F(000)	816	
Absorption coefficient	0.446 mm^{-1}	
Absorption correction	semi-empirical from equivalents	
Max. and min. transmission	0.745 and 0.673	
Theta range for data collection	2.584 to 25.677 deg	
Reflections collected	124473	
Independent reflections	116153 [R_{int} = 0.1133]	
Data / restraints / parameters	116153 / 484 / 462	
wR(F^2 all data)	*wR*2 = 0.2710	
R(*F* obsd data)	*R*1 = 0.0972	
Goodness-of-fit on F^2	1.002	
Observed reflections [I > 2σ(I)]	78171	
Absolute structure parameter	0.13(4)	
Largest and mean shift / s.u.	0.003 and 0.000	
Largest diff. peak and hole	2.879 and -1.554 e/Å^3	

TABLE S1. Crystal parameters and structure refinement.

and minima of 2.879 and -1.554 e/Å^3, respectively. The absolute structure was determined by refinement of the Flack parameter [6]. A summary of the crystal data and structure refinement is given in Table S1.

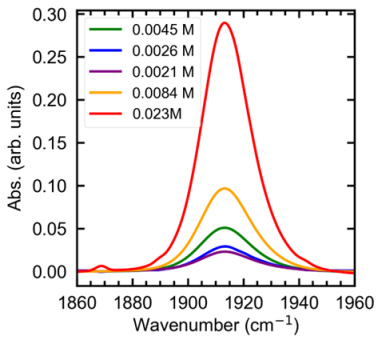

FIG. S1. IR absorption spectra of the (OEP)Ru(CO)(DMPO) carbonyl mode measured in dilute solutions in DCM.

CALCULATION OF $|\vec{\mu}|$ FROM ABSORPTION DATA

We calculate the magnitude of the carbonyl transition dipole based on absorption spectra in solutions of defined concentration through an optical path of known length as described previously [7, 8]. By Beer's Law, the absorbance of the carbonyl vibration is proportional to its molar absorptivity

$$A = \epsilon(\nu)cl, \tag{1}$$

for c the molecular concentration and l the optical path length. The molar absorptivity is then used to calculate the Einstein B coeffieicnt as

$$\int_{-\infty}^{\infty} \epsilon(\nu)d\nu = \frac{N_A h\nu B_{nm}}{\ln(10)}. \tag{2}$$

Finally, the Einstein B coefficient is related to the transition dipole magnitude as

$$B_{nm} = \frac{|\vec{\mu}_{nm}|^2}{6\epsilon_0\hbar^2}. \tag{3}$$

We assume a random orientation of transition dipoles in the solution, which leads to an extra factor of π^2 from integrating the dot product of $\vec{\mu}$ with the electric field as the orientation of $\hat{\mu}$ is varied over all solid angles.

The absorption of the (OEP)Ru(CO)(DMPO) carbonyl mode was measured in five solutions in dichloromethane with concentrations of 23.0, 8.4, 4.5, 2.6, and 2.1 mM using a commercial FTIR spectrometer (Nicolet iS50 Advanced, Thermo Fisher Scientific) and an IR liquid cell (Pike Technologies) with CaF_2 windows and a 0.10 mm spacer. The molar absorptivity, proportional to the absorption spectrum (Fig. S1), is integrated numerically in equation (2). The resulting transition dipole moment is found to be $|\vec{\mu}_{CO}|$ = 1.43 $\pm$ 0.03 D.

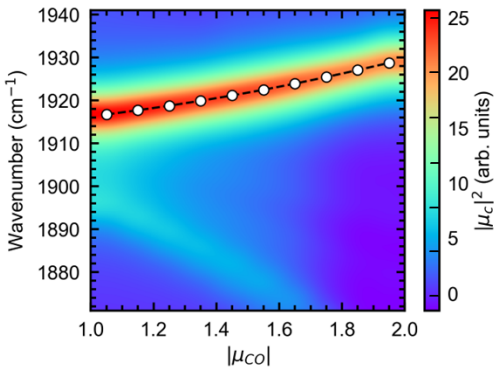

FIG. S2. Theoretical dependence of the modeled collective vibrational spectrum on the transition dipole magnitude, used for uncertainty analysis.

To relate the uncertainty in $|\vec{\mu}|$ to an uncertainty in $\Delta\nu_{mod}$, we calculate the collective vibrational spectrum with $|\vec{\mu}|$ varied from 1.05 to 1.95 D, shown in Fig. S2. The relationship is approximately linear and the uncertainty in $|\vec{\mu}|$ translates to an uncertainty in collective mode energy of 0.4 cm^{-1}.

ADDITIONAL *s*-SNOM EXPERIMENTAL DATA

Nano-FTIR spectra of several polycrystalline aggregates of (OEP)Ru(CO)(DMPO) were measured in addition to the imaged aggregate C1. The peak shifts measured on these aggregates are shown in the main text, Fig. 3C. Here we show additional selected IR *s*-SNOM spectra measured on the eight polycrystalline aggregates exhibiting vibrational coupling in Fig. S3A, as well as spectra on two aggregates which did not exhibit vibrational coupling in Fig. S3B. Aggregates C1-C4 exhibit values of $\Delta\nu$ = (10.4 $\pm$ 0.2) cm^{-1} (within 4% of $\Delta\nu_{mod}$). Aggregates C5-C7 exhibit values of $\Delta\nu$ = (9.7 $\pm$ 0.1) cm^{-1} (within 6% of $\Delta\nu_{mod}$) and aggregate C8 exhibits $\Delta\nu$ = 9.1 cm^{-1}. Values of $\Delta\nu$ are summarized in Table S2.

The aggregates that did not exhibit vibrational mode coupling are likely almost entirely amorphous, with a small shoulder appearing near the coupled frequency for both crystals C9 and C10. Additionally, after exposure to air for longer than one week, all measured spectra resemble those taken on C9 and C10 with the appearance of only one mode near the frequency of isolated molecules. We believe that due to prolonged exposure to air, the molecules become disordered and the crystals degrade into entirely amorphous aggregates.

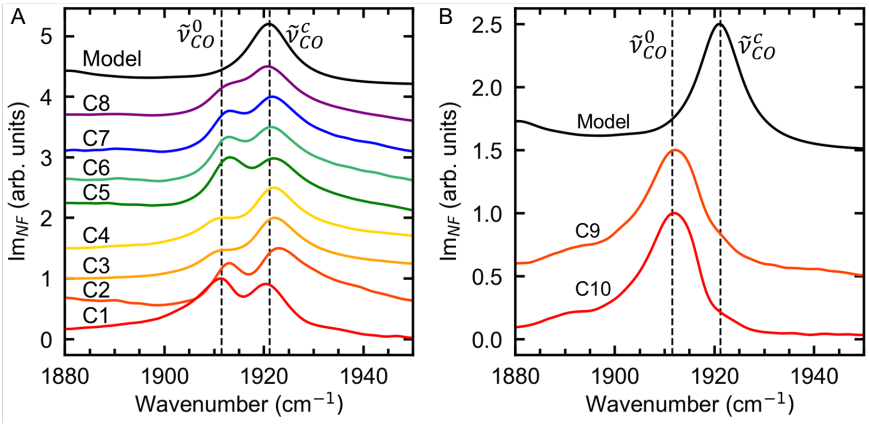

FIG. S3. A) Representative nano-FTIR spectra for all measured polycrystalline aggregates exhibiting vibrational coupling, compared to the modeled collective spectrum (black). B) Near-field spectra for polycrystalline aggregates exhibiting no vibrational coupling, compared to the modeled collective spectrum (black).

Aggregate	C1	C2	C3	C4	C5	C6	C7	C8	C9	C10
$\Delta\tilde{\nu}$ (cm^{-1})	10.33	10.55	10.37	10.37	9.78	9.71	9.67	9.07	NA	NA

TABLE S2. Values of $\Delta\nu$ for all measured aggregates.

MODELING SPECTRA FROM SMALL CRYSTALLINE DOMAINS

We model amorphous domains as composed of a normal distribution of domain sizes with mean domain size $\bar{N}$ and standard deviation σ_N. As illustrated in Fig. 3D in the main text, this distribution is broken into three regions: amorphous domains of single molecules ($N \leq 1$), intermediary domains with $\Delta\nu$ lower than the $N \to \infty$ limit, and large domains with $\Delta\nu$ in the $N \to \infty$ limit ($N > 27$). The area under the normal distribution in each region defines the amplitude of the absorption corresponding to each domain size. For amorphous domains, the center frequency of the absorption is set to 1911 cm^{-1} (N = 1, uncoupled). For large domains, the center frequency is set to 1921.2 cm^{-1} ($N \to \infty$, coupled), as predicted by modeling and measured on domains with seemingly higher average crystalline domain sizes (crystals C1-C4). Intermediate domains have variable values of $\tilde{\nu}$, with $\tilde{\nu}$ shifting linearly between 1911 and 1921.2 cm^{-1} with increasing N. We note that this model is not used to extract the center frequencies of the amorphous and large domains, but rather to deconvolute the spectral contributions from each domain size.

Fits of this model to spectra measured on crystals C5-C8 are shown in Fig. S4, as well as

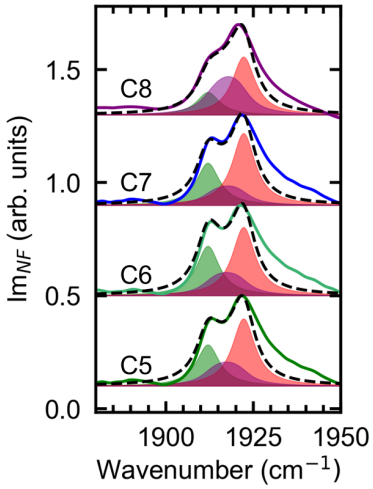

FIG. S4. Fits of Gaussian domain size model to crystal spectra exhibiting values of $\Delta\nu$ lower than 10.2 cm^{-1} when using the two Lorentzian model.

fits to the amorphous region near crystal C1 (points p3 and p4) shown in the main text Fig. 3B. All model fits reproduce the measured collective spectrum to a good approximation, with a large fraction of the spectral response assigned to intermediate domains. The spectra which exhibit a lower $\Delta\nu$ when fitting with the two Lorentzian model (crystal C8 and crystal C1 points p3 and p4) are composed of intermediate domains, whereas crystals C5-C7, which exhibit $\Delta\nu \sim 10$ cm^{-1} have smaller contributions from intermediate domains. This explains the apparent difference in $\Delta\nu$ compared to the Lorentzian fitting being due to the spectral mixing of the intermediate domain response with those of amorphous and bulk crystalline domains. Fit parameters for crystals C5-C8 are $\bar{N}$ = 24, 22, 27, and 23 with σ_N = 40, 45, 50, and 23, respectively.

POLARIZATION DEPENDENCE

The collective vibrational spectrum is composed of two modes, one of which red shifts with increasing domain size (ν_-^c) and the other blue shifts (ν_+^c). The mode ν_-^c is weak in the polarization-averaged spectrum plotted in Fig. 2C, whereas ν_+^c is much stronger and is the only mode observed in experiments. We vary the probe polarization relative to the crystalline domains in our modeling and plot only the component of the collective spectrum polarized parallel to the probe. Since all collective modes are superpositions of uncoupled transition dipoles, all collective modes are in the plane defined by the two transition dipoles shown in Fig. S5A. We can then vary the probe

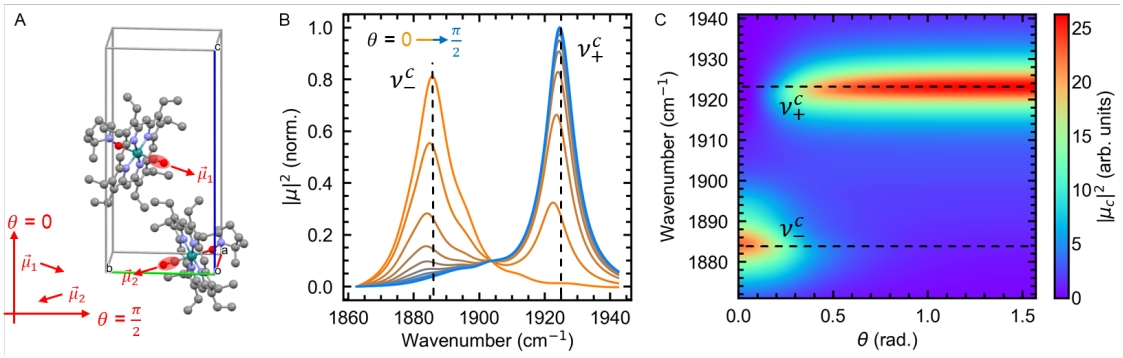

FIG. S5. A) Transition dipole orientations with coordinate system for θ labeled. B) Example spectra for $\sqrt[3]{N}$ = 13 ranging from θ = 0 (orange) to $\theta = \pi/2$ (blue). C) Color plot representing the spectra in B.

polarization angle θ in this plane, with θ = 0 defined as the unit vector along $\vec{\mu}_1 + \vec{\mu}_2$, with $\theta = \pi/2$ along $\vec{\mu}_1 - \vec{\mu}_2$, as shown in Fig. S5A.

As shown in Fig. S5B and S5C, ν_+^c is active when probing along the $\theta = \pi/2$ direction, and is the dominant mode for $\theta > 0.3$ rad. The mode ν_-^c is only active for $\theta < 0.3$ rad, which is the reason it shows up weakly in the polarization-averaged spectrum. All nano-FTIR spectra of (OEP)Ru(CO)(DMPO) polycrystalline aggregates resemble the polarization-averaged spectrum.

VCNC of single crystals thus also allows absolute molecular orientation to be measured rather than relative orientation as was shown here and in previous studies [9–12].

ADDITIONAL MODEL STRUCTURE RESULTS

We model a simple cubic lattice with dipole orientations indicated in Fig. 4A of the main text as an example to derive some general trends, to show the broader applicability to molecular system choices for VCNC studies. As described in the main text, we use this model structure to calculate the dynamic range of VCNC as a function of lattice spacing and transition dipole magnitude. Results for varying lattice spacing are illustrated in Fig. 4C and results of varying transition dipole magnitude are shown in Table S3.

With increasing $|\vec{\mu}|$, we observe only slight changes in k and a clear increase in $\Delta\nu_{max}$ leading to a monotonic increase in l_{max}. We conclude that the dynamic range of VCNC can be maximized by choosing a probe vibration with a large transition dipole magnitude. The calculated l_{max} for $|\vec{\mu}|$ = 1.5 D (the nearest value to that of the carbonyl used here) is 4.93 nm, which is slightly larger than the value of 3 nm predicted for the (OEP)Ru(CO)(DMPO) crystal structure ($\sqrt[3]{N} = 3$, with

	3D			2D		
$\|\vec{\mu}\|$ (D)	k (nm^{-1})	$\Delta\nu_{max}$ (cm^{-1})	l_{max} (nm)	k (nm^{-1})	$\Delta\nu_{max}$ (cm^{-1})	l_{max} (nm)
0.5	0.74	3.32	1.62	0.27	1.39	1.23
1.0	0.73	13.61	3.58	0.26	5.88	6.76
1.5	0.70	30.65	4.93	0.29	13.16	9.05
2.0	0.69	54.50	5.78	0.31	23.12	10.21

TABLE S3. Calculated frequency shift rate k, maximum shift $\Delta\nu_{max}$, and maximum resolvable delocalization length l_{max} for 3D structure in Fig. 4A and corresponding 2D structure with varying $|\vec{\mu}|$ (lattice spacing fixed at a = 1 nm).

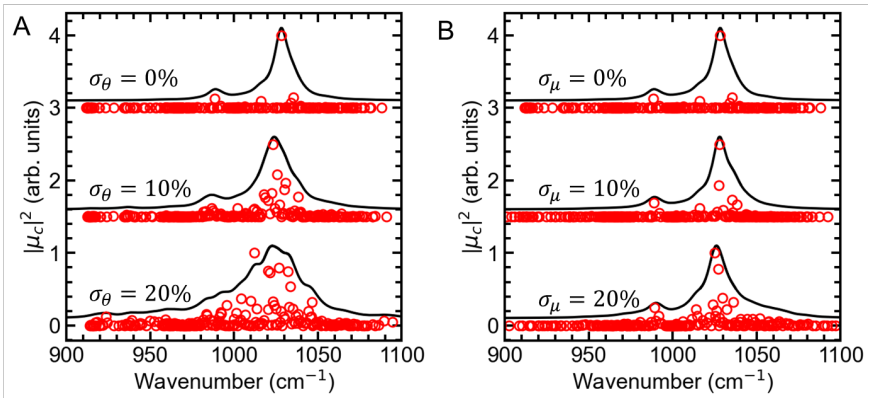

FIG. S6. Calculated IR spectra (black) and corresponding IR activities of each mode (red) for various degrees of disorder in A) transition dipole orientation and B) transition dipole magnitude.

molecular spacings of approximately 1 nm). This shows that knowing the exact crystal structure is important in determining the applicability of VCNC for a given system. The values here are given only to illustrate general trends and estimates of realistic maximum resolvable domain sizes.

The change in collective vibrational spectrum given static disorder in each transition dipole parameter (position, orientation, and magnitude) was also modeled using the example cubic structure. The result of disorder in position is shown in Fig. 4D in the main text for disorder levels of 0%, 10%, and 20% of the ideal lattice spacing of a = 1 nm. That is, each molecule was shifted from its ideal position by a random amount in the x, y, and z directions, with the random displacement chosen for each molecule separately from a normal distribution with standard deviation 0, 0.1, and 0.2 nm, respectively. The same was done for disorder in transition dipole orientation (random disorder added to the dipole angles θ and ϕ with standard deviation given as a percentage

of 90°) and transition dipole magnitude (disorder added to $|\vec{\mu}|$ as a percentage of the ideal value of 2 D), with results shown in Fig. S6.

We observe a similar level of spectral changes for disorder in transition dipole angle as was observed with equal levels of disorder in transition dipole positions. The spectral changes resulting from disorder in transition dipole magnitude are much less pronounced with disorder of 20% of the overall transition dipole magnitude resulting in only minor changes to the overall spectral shape.

---

* markus.raschke@colorado.edu

[1] Lee, J., Twamley, B. & Richter-Addo, G. B. Nitrones are suitable ligands for heme models: X-ray crystal structure of the first metalloporphyrin nitrone complex. *Chem. Comm.* 380–381 (2002).

[2] Muller, E. A., Pollard, B., Bechtel, H. A., van Blerkom, P. & Raschke, M. B. Infrared vibrational nanocrystallography and nanoimaging. *Sci. Adv.* **2**, e1601006 (2016).

[3] Muller, E. A., Pollard, B. & Raschke, M. B. Infrared chemical nano-imaging: Accessing structure, coupling, and dynamics on molecular length scales. *J. Phys. Chem. Lett.* **6**, 1275–1284 (2015).

[4] Krause, L., Herbst-Irmer, R., Sheldrick, G. M. & Stalke, D. Comparison of silver and molybdenum microfocus x-ray sources for single-crystal structure determination. *J. Appl. Cryst.* **48**, 3–10 (2015).

[5] Sheldrick, G. M. Shelxt–integrated space-group and crystal-structure determination. *Acta Cryst.* **71**, 3–8 (2015).

[6] Parsons, S., Flack, H. D. & Wagner, T. Use of intensity quotients and differences in absolute structure refinement. *Acta Cryst.* **69**, 249–259 (2013).

[7] Hollas, J. M. *Modern spectroscopy* (John Wiley & Sons, 2004).

[8] Atkins, P. & de Paula, J. *Physical Chemistry, 5th ed.* (W. H. Freeman and Company, 1994).

[9] Muller, E. A. *et al.* Vibrational exciton nanoimaging of phases and domains in porphyrin nanocrystals. *Proc. Natl. Acad. Sci. U. S. A.* **117**, 7030–7037 (2020).

[10] Mueller, N. S. *et al.* Collective Mid-Infrared Vibrations in Surface-Enhanced Raman Scattering. *Nano Lett.* **22**, 7254–7260 (2022).

[11] Gray, T. P., Nishida, J., Johnson, S. C. & Raschke, M. B. 2D Vibrational Exciton Nanoimaging of Domain Formation in Self-Assembled Monolayers. *Nano Lett.* **21**, 5754–5759 (2021).

[12] Donges, S. A. *et al.* Multidimensional nano-imaging of structure, coupling, and disorder in molecular materials. *Nano Lett.* **21**, 6463–6470 (2021).